Nuclear Science and Techniques (2024) 35:185
https://doi.org/10.1007/s41365-024-01554-7

Research on perturbation of neutron fluence rate in a closed thermal neutron field due to medium materials

Jun-Kai Yang[1] · Ping-Quan Wang[2] · Zhi-Meng Hu[3] · Fan Li[2] · Jun-Mei Zeng[1] · Lin Xiao[1] · Hong-Yu Guo[1] · Jian Zhang[2] · Giuseppe Gorini[4] · Hui Zhang[2] · Chungming Paul Chu[1]

Received: 16 May 2024 / Revised: 24 June 2024 / Accepted: 2 July 2024 / Published online: 1 October 2024

Abstract

The neutron radiation field has vital applications in areas such as biomedicine, geology, radiation safety, and many others for neutron detection and neutron metrology. Correcting neutron fluence rate perturbation accurately is an important yet challenging problem. This study proposes a correction method that analyzes three physical processes. This method, which transforms the detection process from point detection to area detection, is based on a novel physical model and has been validated through theoretical analyses, experiments, and simulations. According to the average differences between the calculated and experimental results, the new method (1.67%) demonstrated better accuracy than the traditional simulation (2.17%). In a closed thermal neutron radiation field, the detector or strong neutron absorption material significantly perturbs the neutron fluence rate, whereas its impact on the energy spectrum shape and neutron directionality is relatively minor. Furthermore, based on the calculation results of the perturbation rate formula for medium materials with different compositions and sizes, the larger the volume and capture cross section of the medium, the higher the perturbation rate generated in the closed radiation field.

Keywords Perturbation rate · Area detection · Three-dimensional neutron energy spectrum · Closed radiation field

1 Introduction

The neutron fluence rate, defined as the number of neutrons entering a small sphere divided by the maximum cross-sectional area during a unit time [1, 2], is one of the most critical physical quantities in neutron metrology because it is closely related to the neutron energy spectrum and neutron dose equivalent [3–5]. Therefore, it is the key comparison quantity for the CCRI (III) (Section III: Neutron measurement of the Consultative Committee on Ionizing Radiation of the International Committee of Weights) [6, 7]. For boron neutron-capture therapy (BNCT) and binary targeted radiotherapy [8–10], the neutron fluence rate is a crucial parameter in treatment-planning systems (TPS) because of the requirement for accurate dose measurement [11–14]. However, in the actual measurement process, because of the absorption and scattering of neutrons by materials of various sizes and compositions, the measurement conditions change after the introduction of medium materials or detectors in the neutron radiation field [15]. This results in changes in the fluence rate, energy spectrum, and neutron

This work was supported by the Fundamental Research Funds of the National Institute of Metrology, China (No. AKYZZ2113), National Key Research and Development Program of China (No. 2017YFF0206205), the Team Building Program of Nanjing University (No. 1480604114).

✉ Hui Zhang
zhanghui@nim.ac.cn

✉ Chungming Paul Chu
pchu@nju.edu.cn

[1] College of Engineering and Applied Sciences, Nanjing University, Nanjing 210093, China

[2] National Institute of Metrology, Beijing 100029, China

[3] Department of Nuclear Science and Technology, Nanjing University of Aeronautics and Astronautics, Nanjing 210093, China

[4] Department of Physics, University of Milan-Bicocca, 20126 Milan, Italy

direction, creating a distorted neutron irradiation field. This distortion is referred to as a perturbation. In particular, fluence rate perturbation is an extremely challenging problem in closed or semi-closed neutron irradiation fields, such as the neutron emission window of BNCT and some reference fields with cavity structures. The neutron fluence rate varies when the measurement position is occupied by a detector or another material [1, 16]. The true value at this position was difficult to obtain from actual measurements because of the presence of real materials. This affects the accuracy of crucial parameter measurements and instrument calibration. Therefore, correcting perturbations in the neutron fluence rate is an important aspect of neutron measurements and neutron metrology.

Over the past century, several theories have been proposed to address this problem [17, 18]. Williams et al. used variational methods to calculate neutron reaction rates in plane foils and subsequently published a series of systematic studies on the neutron fluence rate perturbation caused by infinite plane absorbers [19–22]. Romesburg used diffusion theory and the Monte Carlo method (an unused computer) to study this problem, and the findings showed that the results of the Monte Carlo method were more accurate [23]. However, these studies have stringent requirements for detector shapes and mathematical representations of neutron fluence rates, such as plane detectors and cosine fluence rates, and they require a high level of mathematical and physical knowledge from their users because of their rigor and profundity, thereby limiting their overall applicability.

To address the issue of perturbation of the neutron irradiation field, a joint team from the National Institute of Metrology (NIM), China, and Nanjing University proposed a new and more general physical model. This model is based on systematic physical process analysis, theoretical derivation, and Monte Carlo simulation to obtain the correction factor of the perturbation and verify the theoretical and calculation results against the thermal neutron reference radiation facility in NIM.

2 Theoretical analysis, experiment and simulation

The correction of neutron flux perturbation includes the following three main parts: (1) theoretical analysis of physical processes and establishment of a new physics model, (2) experiments, and (3) Monte Carlo simulation and verification of the results. Each part is described as follows.

2.1 Thermal neutron reference radiation facility

The thermal neutron reference radiation facility was rebuilt after decommissioning the old facility at NIM in 2020. As shown in Fig. 1, 12 ^{241}Am-Be neutron sources were used in this facility to provide two radiation fields: an inner radiation field with graphite moderation and an outer radiation field with heavy water (D_2O) moderation. This new facility exhibits high thermalization and a large distribution of uniformity owing to its innovative design, which includes a reflector layer, homogenizing lenses, and reflective cavities [24].

The inner-field reflective cavity is made of graphite and has dimensions of 72 cm × 72 cm × 27 cm. The neutron fluence rate at the reference point was $(21433.3 \pm 407.2)\ \mathrm{cm}^{-2} \cdot \mathrm{s}^{-1}$, determined by the activation of gold foils, which is an absolute measurement method with a thermal fraction of 94.7% [25], and the uniformity within a linear range of 55 cm was 99%. The outer-field reflective cavity was constructed from polyethylene and measured 90 cm × 90 cm × 65 cm. The neutron fluence rate at the reference point here was $(2046.0 \pm 49.1)\ \mathrm{cm}^{-2} \cdot \mathrm{s}^{-1}$, also determined by the activation of gold foils, with a thermal fraction of 99.96%, and the uniformity within a 70 cm × 70 cm area was more than 99%. Moreover, for the outer radiation field, the key indicators of thermal fraction, uniform area, and uniformity are superior to those of similar devices both domestically and internationally because of the innovative designs mentioned above [26].

2.2 Physical process analysis and physics model establishment

Because the inner and outer radiation field structures are identical, except for the different wall materials, this study takes the reflective cavity of the outer field as an example to analyze physical processes, experiments, and simulations. Furthermore, to help our understanding, the following three physical nomenclatures related to this research are proposed in this paper (these terms are used exclusively in this article).

Perturbation of the neutron irradiation field: Placing a certain volume of material in a neutron radiation field of finite space causes change in the momentum, energy spectrum, or other parameters of the neutron owing to the capture and scattering effects of the material nuclei on the neutron.

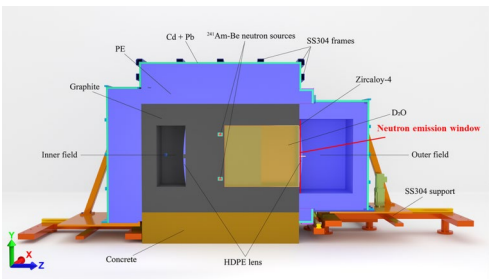

Fig. 1 (Color online) Schematic diagram of the thermal neutron facility [26]

Perturbation rate η: When the irradiation field conditions change, the ratio of the change in a physical quantity at a certain area or point in the field to this quantity with the field unchanged.

Neutron loss rate L: The proportion of neutrons lost per unit time owing to decay, absorption, and other reasons in a closed neutron radiation field.

2.2.1 Neutron transport process of the ^{241}Am-Be neutron source

In the closed neutron radiation field shown in Fig. 1, for example, the neutrons emitted from ^{241}Am–Be neutron sources are moderated by heavy water and reflected by the polyethylene reflector layer. These neutrons are slowed to thermal neutrons that follow the Maxwell distribution and are eventually transported to the emission window [27]. Then, the neutrons emitted from the emission window enter the reflection cavity, where they undergo scattering and capture interactions with the nuclei of the cavity wall material, the nuclei of the detector's sensitive region, or other medium materials. These processes may eventually lead to the dynamic equilibrium of various physical quantities in the neutron field. The same physical processes apply to similar fields.

Therefore, the entire physical process can be decomposed into two steps: a) the neutrons emitted from ^{241}Am–Be neutron sources are moderated in heavy water and transported to the emission window, and b) the neutrons exiting from the window enter the reflection cavity and reach a state of equilibrium with the cavity (as well as the detector or other medium materials). Consequently, if all parameters such as the momentum and energy spectrum of the neutrons in the emission window, can be fully recorded, the entire physical model can be simplified to include only the emission window and reflection cavity. This simplification would greatly improve computational efficiency.

2.2.2 Physical process of neutron entering the reflection cavity

To better understand the temporal evolution of the neutron fluence rate in a closed radiation field, a simplified model was employed for physical analysis. As shown in Fig. 2, assuming that the closed radiation field is surrounded by polyethylene, three physical processes occur when a beam of parallel neutrons enters the reflection cavity: (1) neutrons are captured by interacting with the nuclei of the cavity walls, (2) neutrons are captured by interacting with the nuclei of the cavity walls, and (3) fresh neutrons enter the closed radiation field.

Assuming a unit time interval Δt, the incident neutron count is denoted by φ, and the neutron loss rate is L

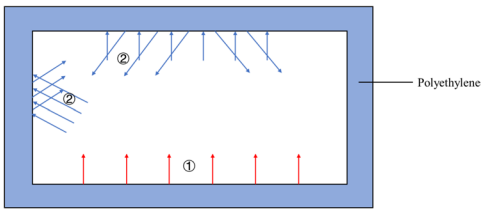

Fig. 2 Schematic diagram of a closed radiation field (①: Neutrons exiting from the window; ②; scattered neutrons produced by the polyethylene walls of the closed radiation field)

$(0 \le L \le 1)$. During the n_{th} time interval Δt_n, a fraction L of the total neutrons present in the reflection cavity from the previous interval Δt_{n-1} was lost, and fresh neutrons with a count of φ were incident from the emission window. The total number of neutrons in the closed radiation field during each time interval can be derived as follows:

First time interval Δt_1:

$$\varphi$$

Second time interval Δt_2:

$$\varphi + \varphi(1 - L)$$

The third time interval Δt_3 :

$$\varphi + (\varphi + \varphi(1 - L))(1 - L)$$

Fourth time interval Δt_4:

$$\varphi + (\varphi + (\varphi + \varphi(1 - L))(1 - L))(1 - L)$$

Therefore, the total number of neutrons of the closed radiation field in n_{th} time interval Δt_n is as follows (Eq. 1):

$$S_n^L = \frac{\varphi[1 - (1 - L)^n]}{L} \quad n = 1, 2, 3, \ldots \tag{1}$$

When the time is sufficiently long, that is, n is sufficiently large (compared with a nuclear reaction time, which is only on the order of 10^{-15} s [28]; a duration of several minutes or even dozens of seconds is considered sufficiently long), the neutron fluence rate in the closed radiation field will inevitably approach a stable value of $\frac{\varphi}{L}$, as shown in Eq. (2):

$$\lim_{n\to\infty} S_n^L = \lim_{n\to\infty} \frac{\varphi[1 - (1 - L)^n]}{L} = \frac{\varphi}{L}. \tag{2}$$

As shown in Fig. 3, introducing medium materials such as Cd or the sensitive region materials of the detector into the closed radiation field will increase the neutron loss rate in the field. We assume that the loss rate under this condition is L_1, where $L_1 > L$. The total number of neutrons within the closed radiation field tended toward a stable value after a relatively long time. According to Eq. (2),

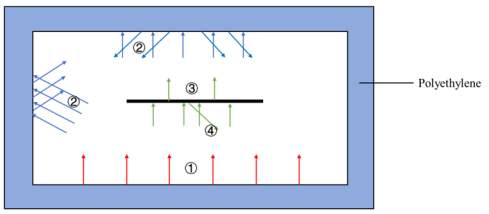

Fig. 3 Schematic diagram of a closed radiation field with medium material present:(①: Neutrons exiting from the window; ②; Scattered neutrons produced by the polyethylene walls of the closed radiation field; ③; Transmitted neutrons after passing through the medium material; ④Scattered neutrons produced by polyethylene walls of the closed radiation field)

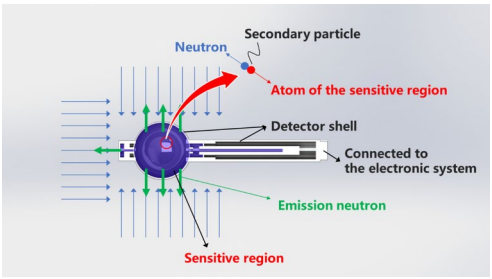

Fig. 4 (Color online) Detailed physical process of neutron detector measurement

the total number of neutrons, as shown in Fig. 3, can be expressed as follows:

$$S_{n_1}^{L_1} = \frac{\varphi}{L_1}$$

Because $L_1 > L$:

$$S_{n_1}^{L_1} < S_n^L$$

As demonstrated by the evidence presented above, in a closed neutron radiation field where the number of neutrons entering the field per unit time remains constant, the total number of neutrons within the field reaches a stable state after a sufficiently long time. However, if a medium with neutron absorption is introduced into the radiation field, increasing the neutron loss rate L, the stable total number of neutrons and the neutron fluence rate within the field will decrease. This results in the perturbation of the radiation field.

2.2.3 Physical process of the neutron detector measurement

The physical process of neutron detector measurements is shown in Fig. 4. Neutrons arriving at the detector pass through the detector shell and enter the sensitive region, where they interact with the nuclei of the sensitive region to produce secondary particles and radiation. Information regarding the neutron fluence can be obtained by detecting the pulse count or current signal of these secondary particles and beams. Neutrons that are not captured exit the sensitive region, and their quantity is related to the capture cross section of the nuclei in the sensitive region. The neutrons measured by the detector at specific points in the radiation field per unit time, divided by the detection efficiency, represent the number of neutrons that enter the sensitive area from the surface. In other words, the starting point of the neutron detection process is the surface of the sensitive region rather than the geometric center of the detector, and the measurement process is the result of area detection rather than point detection. The average surface neutron fluence rate with energy E and direction θ, measured by the detector, can be obtained by integrating the fluence rate at the surface of the sensitive region of the detector and then normalizing it to the area (Eq. 3), which represents the displayed value of the detector.

$$\overline{\varphi(E,\theta)} = \frac{\oint \varphi(E,\theta)\mathrm{d}S}{S}, \tag{3}$$

where $\overline{\varphi(E,\theta)}$ is the normalized neutron fluence rate with energy E and direction θ. $\varphi(E,\theta)$ is the incident neutron fluence rate with energy E and direction θ at the surface of the sensitive region and S is the surface area of the sensitive detector region.

Therefore, according to the definition mentioned above, the perturbation rate $\eta\,(E,\theta)$ caused by the detector is the ratio of the difference between the normalized fluence rate $\overline{\varphi_1(E,\theta)}$ without the detector at the measurement position and the normalized fluence rate $\overline{\varphi_2(E,\theta)}$ with the detector (measurement result) to $\overline{\varphi_1(E,\theta)}$. This is also equivalent to the rate of change in the number of neutrons incident on the surface of the detector-sensitive region, as given by (Eq. 4).

$$\begin{aligned}\eta(E,\theta) &= 1 - \frac{\overline{\varphi_2(E,\theta)}}{\overline{\varphi_1(E,\theta)}} = 1 - \frac{\oint \varphi_2(E,\theta)\mathrm{d}s/S}{\oint \varphi_1(E,\theta)\mathrm{d}s/S} \\ &= 1 - \frac{\oint \varphi_2(E,\theta)\mathrm{d}s}{\oint \varphi_1(E,\theta)\mathrm{d}s} \quad (0 < \theta < \pi)\end{aligned} \tag{4}$$

Therefore, the actual neutron fluenece rate at the measurement position without a detector can be obtained using Eq. (5):

$$\overline{\varphi_1(E,\theta)} = \frac{\overline{\varphi_2(E,\theta)}}{1-\eta(E,\theta)}. \tag{5}$$

To determine the perturbation rate of the neutron fluence rate, counting all the neutrons entering the surface of the detector-sensitive region or medium materials is necessary,

regardless of their energy or direction. The perturbation rate and the actual neutron fluence rate are given by Eqs. (6) and (7), respectively:

$$\eta = \int \eta(E,\theta)\mathrm{d}E\ \mathrm{d}\theta = 1 - \frac{\oint \varphi_2(E,\theta)\mathrm{d}E\ \mathrm{d}\theta\mathrm{d}s}{\oint \varphi_1(E,\theta)\mathrm{d}E\ \mathrm{d}\theta\mathrm{d}s} = 1 - \frac{\oint \varphi_2 \mathrm{d}s}{\oint \varphi_1 \mathrm{d}s} \quad (0 < \theta < \pi), \tag{6}$$

$$\overline{\varphi_1} = \frac{\overline{\varphi_2}}{1-\eta}, \tag{7}$$

where φ_1 and φ_2 are the fluence rates of the incident neutrons with and without the detector at the measurement position and $\overline{\varphi_1}$ and $\overline{\varphi_2}$ are the normalized fluence rates of incident neutrons with and without the detector at the measurement position.

2.3 Experiment

Obtaining the perturbation rate of the occupied positions during the experiment was challenging, so the perturbation rates of the positions were selected to verify the new physics model in the neutron radiation field. The experiment consisted of two steps. First, a thermal neutron detector was used to measure the neutron fluence rate at a set of positions inside the reflection cavity, without any medium. In the second step, the same detector measured the neutron fluence rate at the same positions, but with the addition of the medium material. The change in neutron fluence rate between these two conditions represents the perturbation caused by the introduction of the medium material. The following two principles were considered in selecting the detector and material: (a) the detector should be as small as possible relative to the reflection cavity to minimize perturbation from the detector itself and the coupling between the medium material and the detector; and (b) the medium material should exert some perturbation on the neutron field of the reflection cavity to completely cover the sensitive region of the detector and allow observation of changes in neutron fluence rate as the distance between the detector and the material varies.

The thermal neutron detector, SP9, was manufactured by Centronic Ltd., UK. It has an external diameter of 3.2 cm, the stainless-steel shell that is 1 mm thick, and a nominal pressure of 230 kPa for ^{3}He and 120 kPa for Kr at 20 °C. The influence of SP9 on the neutron radiation field can be neglected because the volume of the detector is only 3×10^{-5} times that of the reflection cavity. For the medium, Cd was selected, with dimensions of 10 cm × 11 cm × 0.1 cm. Cd has an extremely large capture cross section of 19964.1 barns for thermal neutrons (0.0253 eV) and can be considered a perfect blackbody. Other experiments and electronic devices are summarized in Table 1. The measurement time was set to 600 s.

Table 1 Experimental devices

Device	Model
Detector	SP9 (Centronic, UK)
Preamplifier	142PC (Ortec, USA)
Main amplifier	570 (Ortec, USA)
High voltage	556 (Ortec, USA)
Multichannel analyzer	USB-MCA4 CH (TechnoAP, Japan)

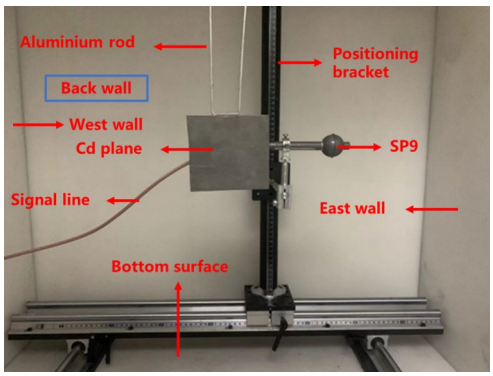

Fig. 5 (Color online) Experimental diagram showing the presence of Cd. (The emission window is parallel to the plane of the paper and is positioned opposite the back wall)

An experiment with Cd and its measurement positions is shown schematically in Fig. 5 and listed in Table 2. The Cd sheet was attached to an aluminum rod with a thermal neutron-capture cross section of 0.233 barns. The geometric center of the Cd sheet was located at the center of the reflection cavity, specifically at (45, 45, 32.5) (45 cm from the bottom, 45 cm from the east wall, and 32.5 cm from the back wall of the cavity, as shown below). The geometric center of the SP9 detector was placed 2.5 cm behind the Cd sheet, at position 1(45, 45, 30). The detector was measured at a single time interval of 300 s with a movement distance interval of 5 cm (toward the east wall). Compared to the initial position, the maximum movement range was 30 cm, whereas other measurement conditions remained unchanged. Moreover, to further understand the perturbation caused by the high-absorption cross-sectional material in the closed radiation field, the neutron fluence rate at position 8(45, 45, 35), which is mirror-symmetric to position 1 with respect to the Cd sheet, was also measured.

Table 2 Measurement position and their corresponding numbers

Number		1	2	3	4	5	6	7	8
Position	East wall	45	40	35	30	25	20	15	45
	Bottom	45	45	45	45	45	45	45	45
	Back wall	30	30	30	30	30	30	30	35

2.4 Monte Carlo simulation

The verification of the physical process analysis and the physics model of perturbation rate in Sect. 2.2 was conducted using MCNP X−2.7.0 (Monte Carlo N-Particle), with the library coupled with ENDF/B-VII. MCNP is a widely used Monte Carlo transport code system in the field of nuclear physics, particularly well-suited for neutron physics calculations, with developments originating from the Los Alamos National Laboratory. Figure 1 shows the geometric configuration of the thermal neutron reference radiation facility. The initial energy spectrum of all ^{241}Am-Be neutron sources were recommended by the International Organization for Standardization 8529-1:2021 [25], and the final energy spectrum inside the stainless-steel capsule were obtained after several iterations of the initial energy spectrum [29, 30]. Thermal neutron scattering $S(\alpha, \beta)(T = 293\,\mathrm{K})$ was applied to the calculation for polyethylene, heavy water, and graphite to account for the elastic scattering processes of neutron energies below 4 eV.

According to the analysis in Sect. 2.2.1, the calculation process is divided into two parts to improve the overall efficiency: a) recording all neutron parameters at the emission window, including energy, location, direction, etc., and b) obtaining parameters at the target location by performing calculations in the reflection cavity, with the emission window acting as a new neutron source. MCNP provides surface source write (SSW) and surface source read (SSR) cards to facilitate these calculations. The SSW card was used to write a surface source file for subsequent MCNP calculations, and the SSR card was used to read the surface source file created with the SSW card. First, the initial calculation sets the global importance factor $IMP = 1$ (shown in Fig. 6a) and uses the SSW card to record the neutron parameters for all S_1 surfaces, including the surface of the emission window (shown in Fig. 6b). Second, we set the importance factor $IMP = 0$ for the S_1 region and $IMP = 1$ for the remaining regions, using the SSR card to read the neutron parameters of the S_1 surface to complete the calculation and verify the new physics model of the perturbation rate. The new method, referred to as area detection based on the analysis in Sect. 2.2.3, is used in the calculation. The F1 card is employed to record the total number of neutrons entering the surface. A ^{3}He sphere, the same component as the sensitive region of SP9, with a diameter of 3.1 cm is placed in the reflecting cavity. The calculation of $\cos\theta$ ranges from −1 to 0 (incident direction: $0 \sim -\pi$), considering 20 blocks. $\cos\theta = -1$ and 0 indicate that the incident neutrons are perpendicular and parallel to the tangent plane of the ^{3}He sphere, respectively. Moreover, to compare the results of different methods and experiments, the traditional simulation method, specifically the F5 card (a point detector model for calculating the neutron flux at an interesting position), was also employed in this study. Based on the measurement positions listed in Table 2 and the actual radius of the SP9 sensitive region, the detector's center and radius (1.55 cm) were set. The perturbation rate can be calculated using Eqs. (4) and (6) after obtaining the neutron flux change.

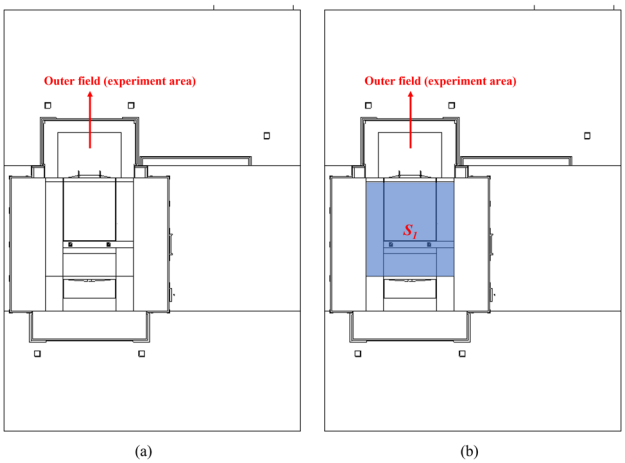

Fig. 6 **a** Distribution of the importance card for the initial calculation in the simulation. **b** Distribution of the importance card for the subsequent calculation in the simulation, Areas with ($IMP = 1$ are shown in white, while areas with $IMP = 0$ are shown in blue)

3 Results and discussion

3.1 The results of the experiment

The experimental measurement results, corrected for dead time, are shown in Fig. 7. As the thermal neutron spectrum corresponds to a Maxwell distribution in the reflection cavity, the response functions $R(E)$ and R_{average} should be constant. According to Eq. (6), the count rate C is proportional to the fluence rate φ. For the condition without the Cd sheet, the variation in the count rate ranged from (6170 ± 11) counts per second (cps) to (6272 ± 11) cps as the SP9

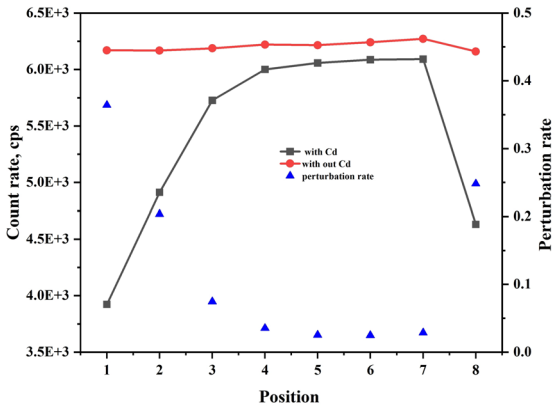

Fig. 7 SP9 count rate at different positions with and without Cd in the reflection cavity

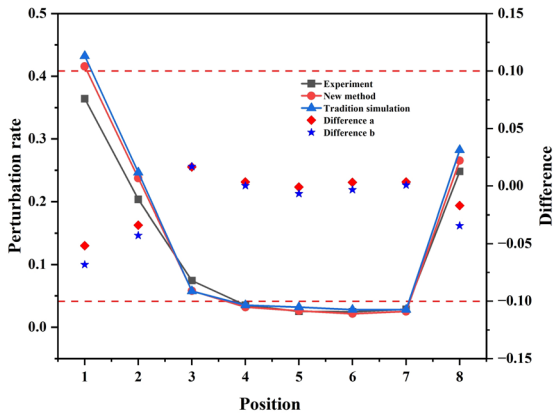

Fig. 8 Perturbation rate of neutron fluence rate from experiments, new method, and tradition simulation after introducing the Cd sheet. Also shown are the differences between these methods: **a** difference between the experiment and new method, and **b** difference between the experiment and traditional simulation)

detector moved from position 1 to position 7, with the count rate being (6159 ± 11) cps at position 8. A nonuniformity of only 0.64% indicates that the neutron fluence rates at all positions were essentially the same in the reflection cavity without Cd. For the condition with the Cd sheet, the count rate ranged from (4631 ± 8) cps at position 1 to (4631 ± 8) cps at position 7, with the count rate being (4631 ± 8) cps at position 8. The nonuniformity was 15.3% in this case, indicating that the introduction of the Cd sheet caused a larger perturbation in the neutron radiation field, and the perturbation rate increased as the detector approached the Cd sheet.

$$C = \int R(E)\varphi(E)\mathrm{d}E = R_{\text{average}}\,\varphi_{\text{total}}\,, \tag{8}$$

where C is the count rate of the SP9 detector, $R(E)$ is the energy response function of the SP9 detector. R_{average} is the average energy response function of the Maxwell distribution, φ_{total} is the total neutron fluence rate at the measurement position in the reflection cavity.

As shown in Fig. 7, the perturbation rate of the experimental results varied from (2.5 ± 0.2)% (position 7) to (36.4 ± 0.2)% (position 1) compared to the condition without the Cd sheet. At position 1, where the geometric center of the detector coincides with that of the Cd sheet and the detector body was completely covered by the Cd sheet, the perturbation of the fluence rate was (36.4 ± 0.2)%, indicating that 63.6% of the neutrons originated from scattering by the reflection cavity walls. The fluence perturbation rate at position 8 was (24.8 ± 0.2)%, which is 11.6% smaller than that at position 1. The two positions were mirror-symmetric about the Cd sheet; neutrons from the emission window and those scattered from the walls were absorbed by the Cd sheet, resulting in an uneven distribution of the neutron fluence rate between the Cd sheet's front and back surfaces. Therefore, in a closed radiation field, if a detector with a large sensitive region is used, the absorption of thermal neutrons by the sensitive region will likely lead to an uneven distribution of the neutron fluence rate on the surface of the sensitive region. In this case, the geometric center of the detector is not an effective measurement center.

3.2 The results of the new method and tradition simulation

Figure 8 shows the perturbation rate at eight positions from the experiment, the new method, and the traditional simulation. All three results show similar trends: the perturbation rates gradually increase as the distance from the Cd sheet decreases. The maximum values for the new and traditional methods were (41.6 ± 0.1) % and (43.2 ± 0.1)% at position 1 and (26.5 ± 0.1) % and (28.2 ± 2.1) % at the mirror-symmetric position 8. Although the differences in perturbation rates between the experiment and the new method, as well as between the experiment and the traditional simulation, were relatively obvious at positions 1, 2, and 8, the absolute values of these differences remained within 10% across all positions, indicating the reliability of the results obtained from both calculations. For positions 3, 4, 5, 6, and 7, the differences *a* and *b* were consistent and close to zero, indicating that the two results were in agreement with the experimental results. The maximum differences, specifically (5.2 ± 0.1)% and (6.8 ± 0.1)%, were observed at position 1, whereas a certain level of deviation was evident at positions 2 and 8 when compared with the experimental results. This observation suggests that the complexity of the radiation field and its proximity to the Cd sheet significantly impact the accuracy of the calculations, with greater complexity and close proximity resulting in more pronounced effects. However, compared to difference b (2.17%), the new method

demonstrated a lower average difference of 1.67%. Both the absolute values and the average difference were smaller, indicating that the calculation results obtained using the new method were more accurate. However, the two values are quite similar, and the difference between the new method and the traditional simulation method can be attributed to the different mathematical and physical neutron statistical methods used in MCNP.

3.3 The perturbation of three-dimensional neutron energy spectrum

As mentioned above, introducing a medium material, particularly one with strong neutron absorption properties such as Cd, into a closed radiation field not only perturbs the total fluence rate but also influences the neutron energy spectrum and direction. The neutron energy spectrum is a critical parameter describing the neutron irradiation field of a radiation source [31–35]. It provides information on the total fluence and the relationship between fluence and energy. Neutrons also exhibit directionality, which is an important physical characteristic in neutron detection. For certain physical quantities, such as the neutron ambient dose equivalent rate and personal dose equivalent rate, the neutron incident direction is a significant parameter, alongside the energy spectrum and fluence-dose equivalent conversion coefficients [36]. The neutron fluence at a specific position φ is defined as the sum of the neutrons of all energies E and incident directions θ: If only the relationship between the neutron fluence and energy, $\varphi(E) \sim E$, is considered, it represents the conventional neutron energy spectrum. However, including the angle in the conventional neutron spectrum allows for constructing a three-dimensional neutron energy spectrum $\varphi(E, \theta) \sim E, \theta$ providing more detailed information about the neutron radiation field. Figures 9 and 10 show the

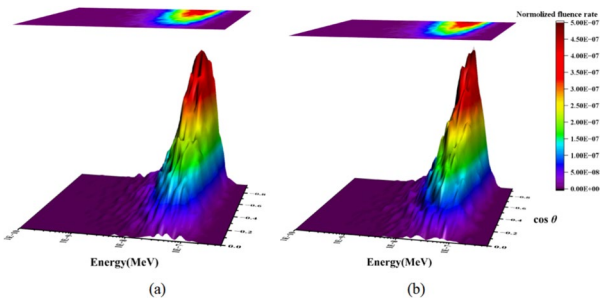

Fig. 9 (Color online) Three-dimensional neutron energy spectrum without the Cd sheet at Position 1 (**a**) and Position 8 (**b**). Note: Due to the inherent drawing constraints of Origin, the neutron fluence rate for $\cos\theta$ in the figure represents the sum of neutron fluence rates within the block in the actual calculation. For example, the neutron fluence rate corresponding to $\cos\theta = -0.95$ in Fig. 9 represents the sum of the neutron fluence rates from $\cos\theta = -1$ to $\cos\theta = -0.95$; this convention applies to similarly to other cases)

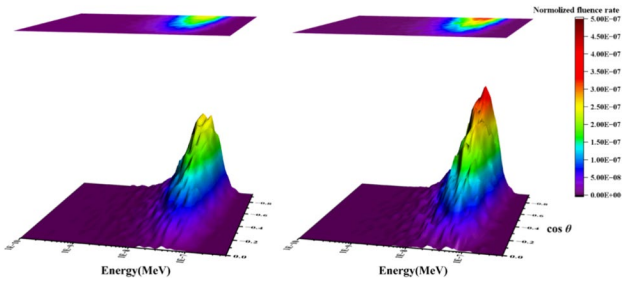

Fig. 10 (Color online) Three-dimensional neutron energy spectrum with the Cd sheet at Position 1 (**a**) and Position 8 (**b**)

three-dimensional neutron energy spectra with and without the Cd sheet at positions 1 and 8. Figure 11 shows the normalized neutron fluence rates for various values of $\cos\theta$. The shapes of these peaks follow the standard thermal neutron spectra, adhering to the Maxwell distribution, and their peak positions are consistent. The number of neutrons entering the detector increased as $\cos\theta$ decreased, with the maximum observed for nearly perpendicular incidence ($\cos\theta$ ranging from -1 to -0.95), accounting for approximately 10% of the total fluence. Moreover, the normalized neutron fluence rate displayed a linear correlation with $\cos\theta$, with the correlation coefficient R^2 exceeding 99.5% in all cases (Fig. 11). Within each $\cos\theta$ interval, the change in the normalized fluence rate with and without the Cd sheet was relatively minor. This indicates that the strong neutron-absorbing material had a limited influence on the neutron direction. While the presence or absence of the Cd sheet had minimal impact on the shape and position of the peak in the reflective cavity, it significantly influenced the neutron fluence rate. Without the sheet, the maximum peak height at position 1 was comparable to that at position 8. Upon introducing the Cd sheet into the reflective cavity, the maximum peak height decreased by $(41.7 \pm 0.1)\%$ at position 1 and $(26.4 \pm 0.1)\%$ at position 8. The difference between these decreases was 15.3%,

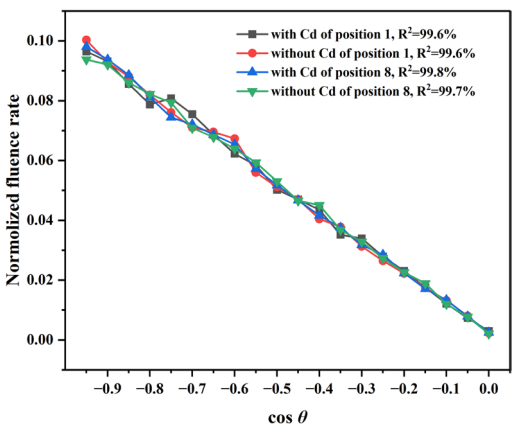

Fig. 11 Normalized neutron fluence rate for various $\cos\theta$ values

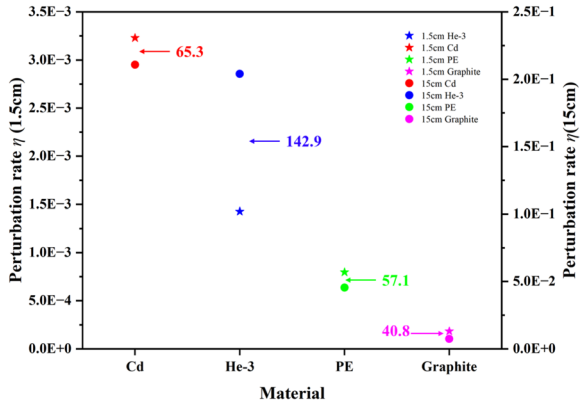

Fig. 12 (Color online) Perturbation rate for different materials and sizes. The number indicate the ratio of the perturbation rate η for each material with diameters of 15 cm and 1.5 cm

which closely aligns with the difference in perturbation rates between the two positions, namely 15.1%, calculated using the new method. Therefore, the perturbation observed in the detector's spectrum within the closed thermal neutron radiation field is mainly associated with changes in the neutron fluence rate rather than alterations in the direction of the measured neutrons or the spectral shape.

3.4 Perturbation rate for different materials and size

According to Eq. (6) and the conclusions mentioned above, the perturbation rates of the neutron fluence rate for four common materials, namely ^{3}He gas (the same as the SP9 component), Cd, polyethylene (PE), and graphite, were calculated in the reflection cavity. To better observe the relationship between material volume and perturbation rate, these materials were assumed to be spherical with diameters of 1.5 cm (3×10^{-5}) times the volume of the reflection cavity) and 15 cm (3×10^{-2}) times the volume of the reflection cavity). As shown in Fig. 12, the perturbation rate η followed the order: $\eta_{\mathrm{Cd}} > \eta_{\mathrm{He\text{-}3}} > \eta_{\mathrm{PE}} > \eta_{\mathrm{Graphite}}$ for both 1.5 cm or 15 cm radius spheres. This order matches the neutron-capture cross-section order for these materials [37]. The ratio of $\eta_{\mathrm{He\text{-}3}(r=15\,\mathrm{cm})}$ to $\eta_{\mathrm{He\text{-}3}(r=1.5\,\mathrm{cm})}$ was 142.9, significantly higher than for the other materials. For a radius of 1.5 cm, the perturbation rate of ^{3}He was only (0.14 ± 0.01)%, indicating that the perturbation caused by the SP9 detector was negligible. η_{Cd} was 2.26 times greater than $\eta_{\mathrm{He\text{-}3}}$ for a radius of 1.5 cm, but only 1.03 times greater for a radius of 15 cm. This discrepancy may be due to the fact that the size of the ^{3}He sphere is much larger than the range of incident neutrons, resulting in the capture of most neutrons entering it. Therefore, the perturbation rate of ^{3}He $\eta_{\mathrm{He\text{-}3}}$ is close to that of Cd η_{Cd}. Furthermore, because the neutron range is related to the capture cross section, a large volume and high capture cross section of the medium result in a significant perturbation rate in a closed thermal neutron radiation field.

4 Conclusion

In this study, systematic and methodological research on the perturbation correction of medium materials in a closed thermal neutron radiation field was conducted. The following conclusions were drawn:

(1) A new physics model and associated formulas are developed to address and correct neutron fluence rate perturbations. This approach transforms the detection process from point detection to area detection and is validated through theoretical derivation, experimentation, and Monte Carlo simulation. The perturbation rate obtained using this method were closer to experimental results compared to traditional simulations and can be applied to other detector shapes. This measurement concept is also significant for detecting other radiation sources such as X-rays or γ-rays, correcting the geometric effects, and determining effective measurement points in an inhomogeneous radiation field.

(2) A three-dimensional neutron energy spectrum was constructed by incorporating neutron directionality, providing more comprehensive information about the radiation field. Analysis of this spectrum revealed that perturbation primarily affects the neutron fluence rate rather than the neutron direction or spectral shape in a closed thermal neutron radiation field.

(3) The perturbation rates of different materials and sizes were analyzed. The results indicated that the perturbation rate is influenced by the capture cross section and size of the medium; the larger the volume and capture cross section of the medium; large volumes and high capture cross sections lead to high perturbation rates in the closed radiation field.

This study is crucial role for improving the accuracy of instrument calibration and material performance evaluations. Moreover, it addresses a key physics problem in the research of closed radiation fields and enhances understanding of radiation field distribution characteristics. Future work will focus on detailed research of perturbation rates with different materials and neutron fields.

Author Contributions All authors contributed to the conception and design of this study. The material preparation, data collection, simulation, and analysis were performed by J-KY, P-QW, ZMH, LJ, MZ, HZ, CPC, and G. The first draft of the manuscript was written by J-KY, P-QW, HZ, CPC, and all authors commented on the previous versions of the manuscript. All the authors have read and approved the final version of the manuscript.

Data availability statement The data that support the findings of this study are openly available in Science Data Bank at https://cstr.cn/31253.11.sciencedb.j00186.00226 and https://www.doi.org/10.57760/sciencedb.j00186.00226.

Declarations

Conflict of interest The authors declare that they have no Conflict of interest.

References

1. D.J. Thomas, R. Nolte, V. Gressier, What is neutron metrology and why is it needed. Metrologia **48**, S225–S238 (2011). https://doi.org/10.1088/0026-1394/48/6/S01
2. X.Y. Liu, X.X. Yu, H.Z. Li et al., Physical design of conversion screens for thermal neutron transmission imaging. Nucl. Tech. **46**, 110203 (2023). https://doi.org/10.11889/j.0253-3219.2023.hjs.46.110203. (**in Chinese**)
3. J.Y. Chen, J.F. Tong, Z.L. Hu et al., Evaluation of neutron beam characteristics for D-BNCT01 facility. Nucl. Sci. Tech. **33**, 12 (2022). https://doi.org/10.1007/s41365-022-00996-1
4. R.J. Zhu, X. Zhou, Z.H. Liu et al., High-precision and wide-range real-time neutron flux monitor system through multipoint linear calibration. Nucl. Sci. Tech. **31**, 94 (2024). https://doi.org/10.1007/s41365-020-00798-3
5. T.N. Le, S.M.T. Hoang, Q.N. Nguyen et al., Evaluation of the calibration factors of neutron dose rate meters in a ^{241}Am-Be neutron field. Nucl. Sci. Tech. **30**, 133 (2019). https://doi.org/10.1007/s41365-019-0654-7
6. S.A. Enger, P.M.A. Rosenschld et al., Monte Carlo calculations of thermal neutron capture in gadolinium: a comparison of geant4 and mcnp with measurements. Med. Phys. **33**, 337–341 (2006). https://doi.org/10.1118/1.2150787
7. C.B. Cláudiaa, M.S. Dias, Application of neural networks for unfolding neutron spectra measured by means of bonner spheres. Nucl. Instrum. Methods **476**, 252–255 (2002). https://doi.org/10.1016/S0168-9002(01)01464-4
8. M. Peng, G.Z. He, Q.W. Zhang et al., Study of neutron production and moderation for sulfur neutron capture therapy. Nucl. Sci. Tech. **30**, 2 (2024). https://doi.org/10.1007/s41365-018-0529-3
9. Y. Zhu, Z. Lin, H. Yu et al., Conceptional design of an adjustable moderator for BNCT based on a neutron source of 2.8 MeV proton bombarding with Li target. Nucl. Eng. Technol. **56**, 1813–1821 (2024). https://doi.org/10.1016/j.net.2023.12.038
10. P. Coghi, J.X. Li, N.S. Hosmane et al., Next generation of boron neutron capture therapy (BNCT) agents for cancer treatment. Med. Red. Rev. **43**, 1809–1830 (2023). https://doi.org/10.1002/med.21964
11. S.H. Jung, I.S. Choi, S.H. Park et al., A new GUI based patient-specific treatment planning system for Boron Neutron Capture Therapy. J. Nucl. Sci. Tech. **45**, 201–204 (2008). https://doi.org/10.1080/00223131.2008.10875822
12. C.M. Lee, H.S. Lee, Development of a dose estimation code for BNCT using GPU accelerated Monte Carlo and collapsed cone convolution methods. Nucl. Eng. Technol. **54**, 1769–1780 (2021). https://doi.org/10.1016/j.net.2021.11.010
13. E. Bavarnegin, A. Sadremomtaz, H. Khalafi et al., Measurement and simulation of the TRR BNCT beam parameters. Nucl. Imstrum. Methods A **830**, 53–58 (2016). https://doi.org/10.1016/j.nima.2016.05.061
14. Advances in Boron Neutron Capture Therapy, International Atomic Energy Agency, Vienna (2023)
15. J.K. Yang, P.Q. Wang, Z.G. Ren et al., Comparison of neutron energy spectrum unfolding methods and evaluation of rationality criteria. Nucl. Sci. Tech. **33**, 164 (2022). https://doi.org/10.1007/s41365-022-01139-2
16. Z.M. Luo, Disturbance of radiation field due to the introduction of detectors into a medium. J. Radiat. Res. Radiat. Proc. **9**(1), 11–16 (1991). (**in Chinese**)
17. R.H. Ritchie, G.R. Dalton, Re: thermal neutron flux depression by absorbing foils and flux perturbations by thermal neutron detectors. Nucl. Sci. Eng. **11**(4), 451–452 (1961). https://doi.org/10.13182/NSE61-A26048
18. J.V. Walker, The effects of flux anisotropy on thermal-neutron flux perturbations. Nucl. Sci. Eng. **22**(1), 94–101 (1965). https://doi.org/10.13182/NSE65-A19766
19. M.M.R. Williams, Neutron flux perturbations due to infinite plane absorbers i. spatially constant source. Proc. Phys. Soc. **85**, 3 (1965). https://doi.org/10.1088/0370-1328/85/3/303
20. M.M.R. Williams, Neutron flux perturbations due to infinite plane absorbers ii: exponential flux. Brit. J. Appl. Phys. **16**, 1841–1852 (1965). https://doi.org/10.1088/0508-3443/16/12/308
21. S.M. Morsy, M.M.R. Williams, Neutron flux perturbations due to infinite plane absorbers iii: Cosine flux. J. Phys. D Appl. Phys. **5**, 1972–1993 (1972). https://doi.org/10.1088/0022-3727/5/11/307
22. M.M.R. Williams, Neutron flux perturbations due to infinite plane absorbers iv: the exponential flux revisited. Nucl. Sci. Eng. **140**, 189–194 (2002). https://doi.org/10.1016/S0168-583X(01)00937-5
23. H.C. Romesburg, *Absorption Induced Thermal Neutron Flux Perturbations* (The University of Arizona, New York, 1962)
24. P.Q. Wang, J.K. Yang, F. Li et al., Thermal neutron reference radiation facility with high thermalization and large uniformity area. Metrologia **60**, 045002 (2023). https://doi.org/10.1088/1681-7575/acd6fb
25. ISO 8529. 2-2000 reference neutron radiations-Part 1: Calibration fundamentals of radiation protection devices related to the basic quantities characterizing the radiation field (2000)
26. J.K. Yang, P.Q. Wang, H. Zhang et al., Experimental measurement of parameters of thermal neutron reference field. Nucl. Tech. **44**, 110501 (2021). https://doi.org/10.11889/j.0253-3219.2021.hjs.44.110501. (**in Chinese**)
27. J.G. Williams, D.M. Gilliam, Thermal neutron standards. Metrologia **48**, S254–S262 (2011). https://doi.org/10.1088/0026-1394/48/6/S03
28. X.T. Lu, *Nucl. Phys. (Revised)* (Atomic Energy Press, Beijing, 2000). (**in Chinese**)
29. C.J. Li, Y.N. Liu, W.H. Zhang et al., Monte Carlo calculation of correction factors for radionuclide neutron source emission rate measurement by manganese bath method. At. Energy Sci. Technol. **48**(10), 1876–1881 (2014). https://doi.org/10.7538/yzk.2014.48.10.1876. (**in Chinese**)
30. J.K. Yang, H. Zhang, P.Q. Wang et al., Parameters of manganese bath measurement device. Nucl. Tech. **45**, 060501 (2022). https://doi.org/10.11889/j.0253-3219.2022.hjs.45.060501. (**in Chinese**)
31. L. Ren, Y.C. Han, J.C. Zhang et al., Neutronics analysis of a stacked structure for a subcritical system with LEU solution driven by a D-T neutron source for ^{99}Mo production. Nucl. Sci. Tech. **32**, 123 (2021). https://doi.org/10.1007/s41365-021-00968-x
32. H.H. Xiong, T.S. Li, S.Z. Chen et al., Investigation of an online reactor neutron spectrum measurement method with ionization chambers. Nucl. Technol. **202**, 94–100 (2018). https://doi.org/10.1080/00295450.2017.1419780
33. Z.M. Hu, Y.H. Zheng, T.S. Fan et al., Experimental evaluation of the Geant4-calculated response functions of a Bonner sphere spectrometer on monoenergetic neutron sources. Nucl. Instrum. Meth. A **965**, 163836 (2020). https://doi.org/10.1016/j.nima.2020.163836
34. S.R. Malkawi, N. Ahmad, Prediction and measurement of neutron energy spectrum in a material test research reactor. Ann. Nucl. Energy **27**, 311–327 (2000). https://doi.org/10.1016/S0306-4549(99)00057-2

35. R. Li, J.B. Yang, X.G. Tuo et al., Unfolding neutron spectra from water-pumping-injection multilayered concentric sphere neutron spectrometer using self-adaptive differential evolution algorithm. Nucl. Sci. Tech. **32**, 26 (2021). https://doi.org/10.1007/s41365-021-00864-4
36. Conversion coefficients for use in radiological protection against external radiation. International Commission on Radiation Units and Measurements (1998)
37. Nuclear Data Services, International Atomic Energy Agency, 25/4/2024. https://www-nds.iaea.org/exfor/endf.htm